Front. Phys. China (2006) 4: 383－395
DOI 10.1007/s11467-006-0049-1

REVIEW ARTICLE

XIE Chang-de, ZHANG Jing, PAN Qing, JIA Xiao-jun, PENG Kun-chi

Continuous variable quantum communication with bright entangled optical beams

Abstract In this paper, we briefly introduce the basic concepts and protocols of continuous variable quantum communication, and then summarize the experimental researches accomplished by our group in this field. The main features of quantum communication systems used in our experiments are: (1) The bright entangled optical beams with the anticorrelated amplitude quadratures and the correlated phase quadratures that serve as the entanglement resources and (2) The Bell-state direct detection systems are utilized in the measurements of quantum entanglement and transmitted signals instead of the usually balanced homodyne detectors.

Keywords quantum communication, entanglement, continuous variables

PACS numbers 03.67.Hk, 42.50.Dv

1 Introduction

In quantum information science, quantum systems are the basic elements for storing, processing and transmitting information. Light is a particularly useful quantum system for communication because it propagates at the maximum speed allowed for the transfer of information. In optical quantum communication the quantum effects of light are utilized. The study of quantum communication involves two kinds of quantum variables used, namely, discrete or continuous. An important difference between the discrete and continuous quantum variables is their representation in terms of superposition of certain basis states. The discrete variables (DV) can be expressed as the superposition of numerous basis states and thus their eigenstates form a finite-dimensional Hilbert space, such as the polarization of a photon, which has a two-dimensional Hilbert space. However, the continuous variables (CV) require an infinite number of basis states and their eigenstates form an infinite-dimensional Hilbert space. Any two different values of a continuous variable correspond to two different eigenstates which are orthogonal, such as the position and momentum of a particle or the amplitude and phase quadratures of an electromagnetic mode. Initially the field of quantum information was proposed and developed in the realm of DV [1] and later was extended to CV [2]. The extension of quantum communication protocols from discrete to continuous variables implies a shift from finite to infinite dimensions.

As Schrödinger put it, the phenomenon of entanglement is one of the quintessential features in quantum mechanics, which has no analogue in classical physics. There are strong nonclassical correlations among the subsystems of a quantum entanglement, even though they may be widely separated. In recent years it has been realized that the nonlocal quantum entanglement is an important resource for quantum information processing. Particularly, many quantum communication schemes rely on the resource of entanglement. Utilizing the entanglement shared between a pair of parties together with local operations and classical communication, various feats of quantum communication can be achieved, which can never be realized only in the frame of classical physics without quantum entanglement. For example, an arbitrary unknown quantum state can be transferred through a classical communication channel to a distant place using a shared entangled pair, that is, quantum teleportation [3－7]; by means of quantum dense coding [8－12], it is possible to extract two classical bits of information from a transmitted quantum bit (qubit) if the sender and receiver share prior entanglement; one may create entanglement between two

XIE Chang-de (✉), ZHANG Jing, PAN Qing, JIA Xiao-jun, PENG Kun-chi
State Key Laboratory of Quantum Optics and Quantum Optics Devices, Institute of Opto-Electronics, Shanxi University, Taiyuan 030006, China
E-mail: changde@sxu.edu.cn

Received September 20, 2006

space-separated systems that have never interacted in the past, called entanglement swapping [13—18]; and the quantum key distribution can be realized by exploiting entanglement established between sender and receiver [19, 20].

The CV entangled states can be efficiently produced using squeezed light, which can be obtained from the nonlinear optical interaction of a laser with a nonlinear crystal inside an optical cavity in an unconditional fashion within every inverse bandwidth time. Besides, the efficient implementation of the essential steps in quantum communication protocols, namely preparation, manipulation, and measurement of quantum states, can be achieved with the mature technologies in quantum optics utilizing continuous amplitude and phase quadratures of the quantized electromagnetic field. Especially, near-unit measurement efficiency for CV of optical field can be provided by homodyne detection. All above-mentioned valuable features motivated us to study CV quantum communication in recent years.

This paper is organized as follows. In Section 2, the experimental system producing CV entangled states with a nondegenerate optical parametric amplifier (NOPA) is presented firstly. A Bell-state direct detection scheme for CV entanglement measurement is introduced in Section 3. Then we summarize the experimental principles and schemes demonstrating CV quantum dense coding, controlled dense coding and unconditional entanglement swapping in Section 4,5, and 6, respectively. Finally, a brief conclusion is given in Section 7.

2 Generation system of bright entangled optical beams

The various experiments have demonstrated that the entangled optical field can be obtained by combining two independent squeezed vacuum fields produced from a subthreshold degenerate optical parametric amplifier (DOPA) [7, 21, 22]. More straightforward, Einstein-Podolsk-Rosen (EPR) entangled optical beams can be generated from a nondegenerate optical parametric amplifier (NOPA), in which a type-II phase-matched $\chi^{(2)}$ nonlinear optical crystal is involved [23—26]. By injecting a pair of frequency-degenerate and polarization-orthogonal subharmonic seed waves into a NOPA with a harmonic pump power below its oscillation threshold, the bright EPR beams will be produced through an intracavity frequency-down-conversion process. When the NOPA is operated at the state of amplification, namely the injected seed waves and the pump laser are in phase, the output optical field is bright EPR entangled beams with correlated amplitude quadratures and anticorrelated phase quadratures [26]. In the other case, if the NOPA is operated at the state of deamplification, that is, the seed waves and the pump laser are out of phase with a phase difference of π, the bright EPR beams with anticorrelated amplitude quadratures and correlated phase quadratures will be obtained [12].

The amplitude $(\hat{X}_1, \hat{X}_2)$ and phase $(\hat{Y}_1, \hat{Y}_2)$ quadratures of the output signal and idler optical modes from a NOPA are expressed by the following equations [23, 24, 27]:

$$\begin{aligned} \hat{X}_1 &= \hat{X}_{01}\cosh\gamma \pm \hat{X}_{02}\sinh\gamma \\ \hat{Y}_1 &= \hat{Y}_{01}\cosh\gamma \mp \hat{Y}_{02}\sinh\gamma \\ \hat{X}_2 &= \hat{X}_{02}\cosh\gamma \pm \hat{X}_{01}\sinh\gamma \\ \hat{Y}_2 &= \hat{Y}_{02}\cosh\gamma \mp \hat{Y}_{01}\sinh\gamma \end{aligned} \tag{1}$$

where $\hat{X}_{01}$, $\hat{X}_{02}$, and $\hat{Y}_{01}$, $\hat{Y}_{02}$ are the amplitude and phase quadratures of the signal and idler seed waves injected into the NOPA, respectively; γ is the correlation (also named squeezing) parameter that depends on the strength and the time of parametric interaction and is a positive real quantity ($0 \leqslant \gamma < +\infty$); two sets of the plus and minus symbols at upper or lower in Eq. (1) correspond to the state of NOPA operating at amplification or deamplification, respectively. If the injected seed waves are coherent light with $\left\langle \hat{X}_{01}^2 \right\rangle = \left\langle \hat{Y}_{01}^2 \right\rangle = \left\langle \hat{X}_{02}^2 \right\rangle = \left\langle \hat{Y}_{02}^2 \right\rangle = 1$ and their losses in the NOPA are balanced, the normalized fluctuation variables of the quadratures for the individual output modes 1 and 2 as well as the quantum correlation variances between the two modes are calculated from Eqs. (1), respectively:

$$\begin{aligned} &\left\langle \delta^2 \hat{X}_1 \right\rangle = \left\langle \delta^2 \hat{Y}_1 \right\rangle = \left\langle \delta^2 \hat{X}_2 \right\rangle = \left\langle \delta^2 \hat{Y}_2 \right\rangle \\ &\quad = \cosh^2\gamma + \sinh^2\gamma = \cosh(2\gamma) = \frac{\mathrm{e}^{2\gamma} + \mathrm{e}^{-2\gamma}}{2} \end{aligned} \tag{2}$$

$$\left\langle \delta^2 \left(\hat{X}_1 \mp \hat{X}_2 \right) \right\rangle = \left\langle \delta^2 \left(\hat{Y}_1 \pm \hat{Y}_2 \right) \right\rangle = 2\mathrm{e}^{-2\gamma} \tag{3}$$

Generally, the correlation parameter γ is a function of the noise frequency (Ω). The signals modulated on a quadrature of an optical mode at a given radio frequency (RF) can be considered as artificial noise $\delta X_s(\Omega)$ or $\delta Y_s(\Omega)$ in quantum communication. From Eqs. (2) and (3) we can see, the larger the parameter γ, the better the correlation between modes 1 and 2. When $\gamma = 0$, the variance of each single beam [Eq. (2)] equals 1 (the normalized shot noise limit SNL) and the correlation variance [Eq. (3)] equals 2 (the sum of two SNL). When $\gamma \to \infty$, the variance of a single beam tends to infinity and the correlation variance tends to zero. $\gamma = 0$, $\gamma > 0$, and $\gamma \to \infty$ correspond to no correlation, partial correlation, and perfect correlation, respectively. Of course, the ideal limit of $\gamma \to \infty$ cannot be reached in experiments because it requires infinite squeezing of optical field and thus infinite energy. However, the advantages of CV quantum communication only using reachable quantum correlation over classically optical communication have been proved by a number of experimental and theoretical publications [2].

The schematic of an experimental setup generating bright EPR entangled optical beams used in our quantum communication systems is shown in Fig. 1. The entangled EPR beams are generated from a NOPA consisting of an α-cut type-II KTP ($KTiOPO_4$, Potassium Titanyl Phosphate) crystal (10 mm long) and a concave mirror (M) in a semi- monolithic configuration. The front face of the KTP crystal is coated to be used for the input coupler (the transmissions of > 95 % at 540 nm of the harmonic wavelength and ≈ 0.5 % at 1080 nm of the subharmonic wavelength) and the other face is coated with the dual-band antireflection at both 540 nm and 1080 nm. The concave mirror of 50 mm-curvature radius serves as the output coupler of EPR beams at 1080nm and high reflectivity at 540 nm, which is mounted on a piezoelectric transducer to lock actively the cavity length on resonance with the injected seed waves at 1080 nm using the standard FM sideband technique. By fine-tuning the length of the cavity of NOPA and the temperature of the KTP crystal the birefringence between signal and idler waves in KTP can be compensated and the double resonance of them in the cavity can be completed. The process of adjusting the temperature to meet double resonance may be monitored with an oscilloscope while slowly scanning the length of the cavity. Once the double resonance of the two subharmonic waves with orthogonal polarizations is realized, the NOPA is locked on the frequency of the injected seed waves [26]. The measured finesse, the free spectral range, and the line-width of the optical cavity of the NOPA are 110, 2.8 GHz, and 26 MHz, respectively.

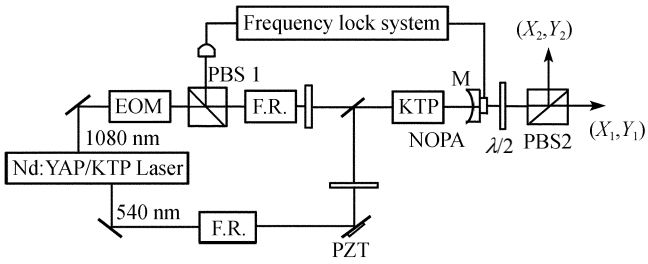

Fig.1 Experimental setup for the generation of EPR beams. Nd: YAP/KTP — Pump laser, KTP — Nonlinear crystal in NOPA, F.R. — Faraday rotator, EOM — Electric optical modulator, PBS — Polarizing beam splitter.

The pump source (Nd:YAP/KTP) is a home-made all-solid-state intracavity-frequency-doubled and frequency-stabilized cw ring laser (Nd:YAP, Yttrium Aluminum Perovskite) [28]. The output harmonic wave at 540 nm and the leaking subharmonic wave at 1080 nm are utilized as the pump laser and the seed waves of the NOPA, respectively. The laser-diode-pumped all-solid-state laser and the semi-monolithic Fabre-Perot configuration of the NOPA cavity ensure the stability of the optical system, in order that the frequencies and the phases of the optical waves can be well-locked during experiments.

The pump power of NOPA at 540 nm should be controlled below the oscillation threshold of the NOPA to avoid multimodes oscillation, and the polarization of the pump wave should be along the b axis of the KTP crystal to meet the requirement for type II phase-matching. Due to the large transmission (> 95 %) of the input coupler at 540 nm, the pump field only passes the cavity twice and does not resonate. To obtain the balanced signal and idler seed waves ($\hat{X}_{01}, \hat{Y}_{01}$, and $\hat{X}_{02}, \hat{Y}_{02}$) inside the KTP crystal, the injected seed optical beam should be polarized to 45° relative to be the signal and idler seed waves with an identical intensity and orthogonal polarizations along the *b* and *c* axes, respectively. The temperature of the KTP crystal placed in a specially designed oven is actively controlled around the temperature for achieving type II noncritical phase matching (~ 63 ℃) with a broad full width of about 30 ℃. An electronics feedback circuit is employed to stabilize actively the temperature fluctuation of the crystal within a few mk.

Locking the relative phase between the pump laser and the injected seed beam of NOPA to $2n\pi$ or $(2n+1)\pi$ (n is any integer) to enforce the NOPA operating at amplification or deamplification, the bright EPR entangled optical beams with the correlated amplitude (or phase) quadratures and the anticorrelated phase (or amplitude) quadratures are generated from the NOPA. The two halves of the output EPR beams are just the signal and idler modes of the subharmonic optical field produced from the type II parametric down-conversion; thus they have orthogonal polarizations originally. The output signal ($\hat{X}_1, \hat{Y}_1$) and idler beams ($\hat{X}_2$, $\hat{Y}_2$) are separated by a polarizing-beam-splitter (PBS2). The two space-separated optical modes ($\hat{X}_1, \hat{Y}_1$) and ($\hat{X}_2, \hat{Y}_2$) are a pair of EPR beams, which possess the feature of nonlocal quantum entanglement of the amplitude and phase quadratures.

3 Direct measurement of Bell-state

Another important task in quantum communication is the measurement of entanglement. Usually the homodyne detection applied in phase-sensitive measurements of electromagnetic field quadratures are used in the measurement of optical CV entanglement [7, 21, 22]. However, for performing the homodyne detection the local oscillator (LO) is needed and the well spatial and temporal mode matching between the LO and the detected beam is required, which is troublesome for experimental implementation. For avoiding the difficulties, we proposed a direct measurement scheme of CV entanglement for bright entangled optical beams with anticorrelated amplitude quadratures and correlated phase quadratures, which was named the direct measurement of Bell-state [11].

The diagram of the direct measurement system is shown in Fig. 2. Two bright coherent optical beams with identical

intensities are expressed by the annihilation operators $\hat{a}$ and $\hat{b}$. A phase shifter is placed in the path of $\hat{a}$ to impose a phase difference of $\pi/2$ between $\hat{a}$ and $\hat{b}$ before they are mixed on a 50 % beam splitter (BS). The resulting output beams $\hat{c}$ and $\hat{d}$ are given by:

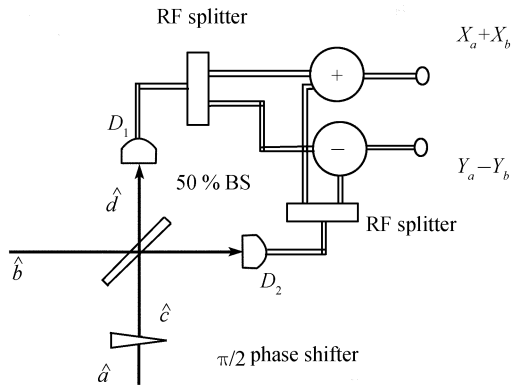

Fig. 2 Direct measurement of Bell-state. BS: 50 % beam splitter; D1 and D2: photoelectric detector; RF splitter: radio frequency splitter; $\pi/2$ phase shiftter: $\pi/2-\pi/2$ phase shiftter; $\oplus$ and $\ominus$: positive and negative power combiner.

$$\begin{aligned}\hat{c} &= \frac{1}{\sqrt{2}}\left(\hat{a}+\mathrm{i}\hat{b}\right)\\ \hat{d} &= \frac{1}{\sqrt{2}}\left(\hat{a}-\mathrm{i}\hat{b}\right)\end{aligned} \tag{4}$$

The operators $\hat{a}, \hat{b}, \hat{c}$, and $\hat{d}$ stand for the amplitudes of the corresponding optical field with a centre frequency ω_0 under the rotating-wave approximation, which is a slowly varying function in time t. The operators are expressed with a unified symbol $\hat{O}(t)$ in the following. By the Fourier transformation we have

$$\hat{O}(\Omega) = \frac{1}{\sqrt{2\pi}}\int \hat{O}(t)\mathrm{e}^{\mathrm{i}\Omega t}\mathrm{d}t \tag{5}$$

The commutators of $\hat{O}$ are

$$\begin{aligned}\left[\hat{O}(t),\hat{O}^{+}(t')\right] &= \delta(t-t')\\ \left[\hat{O}(\Omega),\hat{O}^{+}(\Omega')\right] &= \delta(\Omega-\Omega')\end{aligned} \tag{6}$$

The electromagnetic field can be considered to be composed of a coherent carrier at the centre frequency ω_0, $\hat{O}(\omega_0)$, and the noise sidebands, $\hat{O}(\omega_0 \pm \Omega)$. The average photon numbers of $\hat{O}(\omega_0)$ are a steady value:

$$\left\langle \hat{O}(\omega_0)\right\rangle = \left\langle \hat{O}\right\rangle \tag{7}$$

and the average value of the noise sidebands equals zero

$$\left\langle \hat{O}(\omega_0 \pm \Omega)\right\rangle = 0 \tag{8}$$

The amplitude and phase quadratures of the field $\hat{O}(\Omega)$ are expressed by:

$$\begin{aligned}\hat{X}_0(\Omega) &= \hat{O}(\Omega)+\hat{O}^{+}(-\Omega)\\ \hat{Y}_0(\Omega) &= -\mathrm{i}\left[\hat{O}(\Omega)-\hat{O}^{+}(\Omega)\right]\end{aligned} \tag{9}$$

The commutator of $\hat{X}_0$ and $\hat{Y}_0$ is

$$\left[\hat{X}_0(\Omega),\hat{Y}_0(\Omega)\right] = \mathrm{i}\delta(\Omega+\Omega') \tag{10}$$

The two bright output beams, $\hat{c}$ and $\hat{d}$, are directly detected by the detectors D_1 and D_2. The output photocurrents spectra normalized to the average value of the field are given by

$$\begin{aligned}\hat{i}_c(\Omega) &= \frac{1}{\langle c\rangle}\int \hat{c}^{+}\hat{c}\mathrm{e}^{-\mathrm{i}\Omega t}\mathrm{d}t\\ &= \frac{1}{2\langle c\rangle}\int\left(\hat{a}^{+}\hat{a}+\mathrm{i}\hat{a}^{+}\hat{b}-\mathrm{i}\hat{b}^{+}\hat{a}+\hat{b}^{+}\hat{b}\right)\mathrm{e}^{-\Omega t}\mathrm{d}t\\ &= \frac{1}{2\langle c\rangle}\int\left[\hat{a}^{+}(\omega-\Omega)\hat{a}(\omega)+\mathrm{i}\hat{a}^{+}(\omega-\Omega)\hat{b}(\omega)\right.\\ &\quad \left.-\mathrm{i}\hat{b}^{+}(\omega-\Omega)\hat{a}(\omega)+\hat{b}^{+}(\omega-\Omega)\hat{b}(\omega)\right]\mathrm{d}\omega\end{aligned} \tag{11}$$

Taking $\omega = \Omega$, 0, $-\Omega$ and using Eq. (10), we obtain

$$\hat{i}_c(\Omega) = \frac{1}{2}\left[\hat{X}_a(\Omega)+\hat{Y}_a(\Omega)-\hat{Y}_b(\Omega)+\hat{X}_b(\Omega)\right] \tag{12}$$

In the same way we have

$$\begin{aligned}\hat{i}_d(\Omega) &= \frac{1}{\langle d\rangle}\int \hat{d}^{+}\hat{d}\mathrm{e}^{-\mathrm{i}\Omega t}\mathrm{d}t\\ &= \frac{1}{2}\left[\hat{X}_a(\Omega)-\hat{Y}_a(\Omega)+\hat{Y}_b(\Omega)+\hat{X}_b(\Omega)\right]\end{aligned} \tag{13}$$

Since a phase difference of $\pi/2$ is added between $\hat{a}$ and $\hat{b}$, not only the amplitude quadratures $\hat{X}_a(\Omega)$ and $\hat{X}_b(\Omega)$ but also the phase quadratures $\hat{Y}_a(\Omega)$ and $\hat{Y}_b(\Omega)$ are involved in $\hat{i}_c$ and $\hat{i}_d$. Each of the photocurrents $\hat{i}_c$ and $\hat{i}_d$ is divided into two parts through the RF (radio frequency) power splitter. The sum and difference of the divided photocurrents are

$$\hat{i}_{+}(\Omega) = \frac{1}{\sqrt{2}}\left[\hat{i}_c(\Omega)+\hat{i}_d(\Omega)\right] = \frac{1}{\sqrt{2}}\left[\hat{X}_a(\Omega)+\hat{X}_b(\Omega)\right] \tag{14}$$

$$\hat{i}_{-}(\Omega) = \frac{1}{\sqrt{2}}\left[\hat{i}_c(\Omega)-\hat{i}_d(\Omega)\right] = \frac{1}{\sqrt{2}}\left[\hat{Y}_a(\Omega)-\hat{Y}_b(\Omega)\right] \tag{15}$$

We can see that the sum and difference photocurrents, $\hat{i}_{+}$ and $\hat{i}_{-}$, only retain the amplitude and phase quadratures of $\hat{a}$ and $\hat{b}$, respectively; thus the fluctuation variance of $\hat{i}_{+}$, $\left\langle \delta^2(\hat{X}_a+\hat{X}_b)\right\rangle$, is just the measurement of the amplitude anticorrelation between $\hat{a}$ and $\hat{b}$, and that of $\hat{i}_{-}$, $\left\langle \delta^2(\hat{Y}_a-\right.$

$\hat{Y}_b)\rangle$, is the measurement of the phase correlation. It means that by using the simply direct detection, the CV Bell-state measurement of the bright optical field can be achieved.

Figure 3 shows the quantum correlations between the amplitude and phase quadratures of EPR beams measured by the Bell-state detector [12]. Both the measured variances of $\langle \delta^2(\hat{X}_a + \hat{X}_b)\rangle$ and $\langle \delta^2(\hat{Y}_a - \hat{Y}_b)\rangle$ are ~ 4 dB below the SNL. Considering the electronic noise that is 8 dB below the SNL, the actual fluctuation variance should be ~ 5.4 dB below the SNL; hence the product of the correspondent conditional variance of the EPR beams is $\langle \delta^2(\hat{X}_a + \hat{X}_b)\rangle\langle \delta^2(\hat{Y}_a - \hat{Y}_b)\rangle$ = 0.63. The intensity of the EPR beams was ~70 μw, which was generated from a NOPA operating at deamplification under a pump power of ~ 150 mW below the oscillation threshold of ~ 175 mW and a seed wave with an intensity of ~ 10 mW before entering the input coupler of the NOPA. The SNL was obtained by substituting two independent coherent lights of identical intensity for $\hat{a}$ and $\hat{b}$.

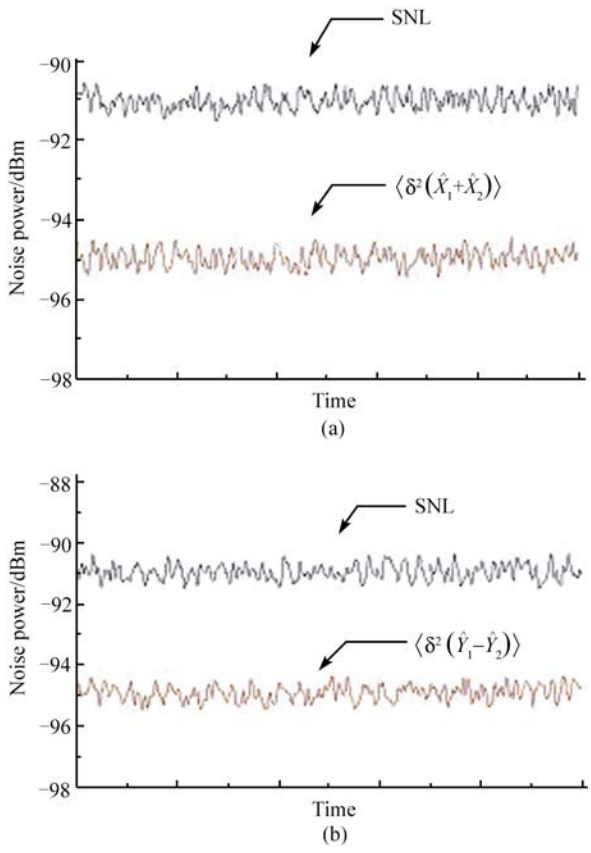

Fig. 3 Spectral densities of photocurrent fluctuations $\langle \delta^2(X_1 + X_2)\rangle$ **(a)** and $\langle \delta^2(Y_{1_1} - Y_{2_2})\rangle$ **(b)**. SNL: the shot noise limit. Acquisition parameters: radio frequency (RF) $\Omega/2\pi$ = 2 MHz, resolution bandwidth $\Delta\Omega/2\pi$ = 30 kHz, video bandwidth 0.1 kHz; the electronics noise is ~ 8 dB below the SNL.

4 Quantum dense coding of continuous variables

Quantum teleportation and quantum dense coding are two typical examples exploiting nonlocal quantum correlations of entangled states in quantum information to perform otherwise impossible tasks. Quantum dense coding provides a method by which two bits of classical information can be transmitted by sending a qubit. The dense coding, originally proposed [8] and successively experimentally demonstrated [9], is concentrated within the setting of discrete quantum variables. Later, the schemes realizing highly efficient dense coding are theoretically proposed, in that the two-mode squeezed-state entanglement is exhibited to achieve unconditional signal transmission [10, 11]. In 2002, the first CV dense coding was experimentally demonstrated by using the bright EPR optical beams produced from a NOPA operating at deamplification [12]. The experimental schematic is shown in Fig. 4.

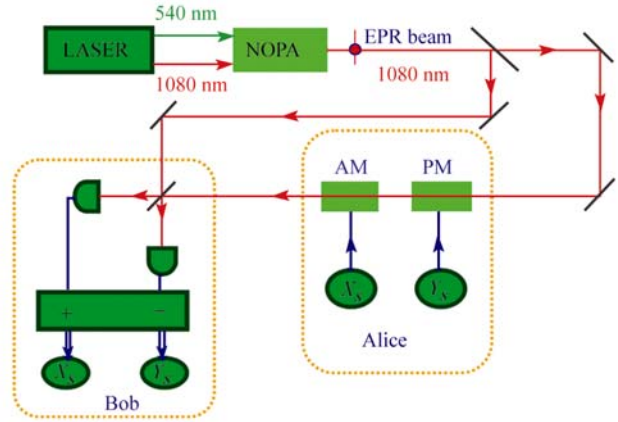

Fig. 4 Schematic of the experimental apparatus for dense coding of continuous variables. Two bits of classical information X_s and Y_s are encoded on the amplitude and phase quadratures of a half of EPR beams (beam 1) at Alice, then are decoded by the other half of the EPR beams (beam 2) at Bob.

The two halves (beam 1 with quadratures $\hat{X}_a, \hat{Y}_a$ and beam 2 with quadratures $\hat{X}_b, \hat{Y}_b$) of the EPR entangled optical be- ams were distributed to the sender Alice and the receiver Bob, respectively. At Alice, two sets of classical amplitude and phase signals, were simultaneously modulated on the beam 1, which led to the displacement of the amplitude quadrature and the phase quadrature, respectively. Since each half of the EPR beams had huge quantum noises on the quadratures individually, the signal-to-noise ratios (SNR) in beam 1 for both amplitude and phase signals were very low. However, at Bob the signals were decoded with the Bell-state direct detector under the aid of the other half of the EPR beams (beam 2), which was combined with the modulated beam 1on a 50 % beam splitter. From Eqs. (14) and (15), the sum and difference photocurrents become

$$\hat{i}_+ = \frac{1}{\sqrt{2}}[\hat{X}_a(\Omega) + \hat{X}_b(\Omega) + \hat{X}_s(\Omega)] \tag{16}$$

$$\hat{i}_{-}=\frac{1}{\sqrt{2}}[\hat{Y}_a(\Omega)-\hat{Y}_b(\Omega)+\hat{Y}_s(\Omega)] \tag{17}$$

where $\hat{X}_s(\Omega)$ and $\hat{Y}_s(\Omega)$ are the amplitude and phase signals modulated on beam 1 with the modulation frequency Ω. Both encoded amplitude and phase signals will be recovered with a sensitivity beyond that of the SNL when the beam 1 and beam 2 are quantum entangled, that is, $\left\langle\delta^2(\hat{X}_a+\hat{X}_b)\right\rangle <$ SNL and $\left\langle\delta^2(\hat{Y}_a-\hat{Y}_b)\right\rangle <$ SNL. Figure 5 shows the directly measured amplitude (a) and phase (b) signals at Bob , which are the signals at 2 MHz modulated on beam 1 by the amplitude (AM) and phase (PM) modulators at Alice. We can see that the original signals are retrieved with the high SNRs of ~ 4 dB and ~ 3.6 dB beyond that of the SNL under the help of beam 2, respectively (accounting for the electronics noise of ~ 8 dB below the SNL, the actual values should be ~5.4 dB and ~ 4.8 dB, respectively). In this experiment, the simultaneous measurements of the amplitude and phase signals are achieved both with the precision beyond that of the SNL by means of exploiting the CV EPR entanglement.

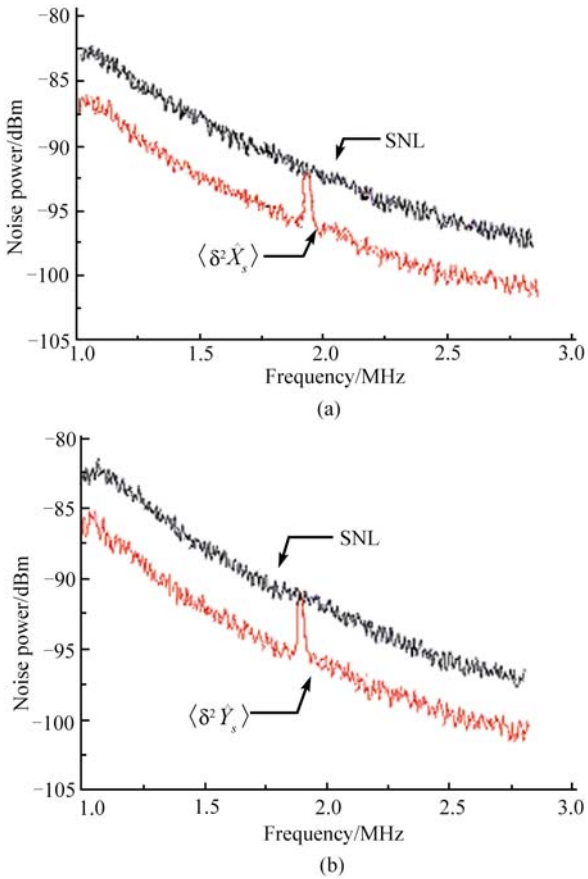

Fig. 5 Measured amplitude **(a)** and phase signal **(b)** at Bob, when EPR beam 1 is phase- and amplitude-modulated at 2 MHz at Alice. SNL: the shot noise limit. Acquisition parameters: measured frequency range 1.0—3.0 MHz, resolution bandwidth 30 kHz, video bandwidth 0.1 kHz; the electronics noise is ~ 8 dB below the SNL.

In Ref. [10], Braustein and Kimble theoretically proved that for a constraint in the mean number of photons ($\bar{n}$) associated with modulation in the signal channel, the optimized channel capacity of CV dense coding equals

$$C_{\mathrm{dc}}^{\mathrm{opt}}=\ln(1+\bar{n}+\bar{n}^2) \tag{18}$$

Generally , the mean number of photons involved in a half of EPR beams with modulated signals is expressed by [27]:

$$\bar{n}=\sigma^2+\sinh^2\gamma \tag{19}$$

where γ is the squeezing (or correlation) parameter mentioned above, and $\sinh^2\gamma$ and σ^2 stand for the photon numbers occupied by the squeezed noise sideband of an optical field and the modulated signals, respectively. For a fixed $\bar{n}$, the condition for achieving the optimal information throughput $C_{\mathrm{dc}}^{\mathrm{opt}}$ of the dense coding channel is [10]:

$$\bar{n}=\mathrm{e}^r\sinh\ \gamma \tag{20}$$

taking

$$\sigma^2=\sinh\ r\cdot\cos\ \gamma \tag{21}$$

For large squeezing r the Eq. (18) becomes

$$C_{\mathrm{dc}}^{\mathrm{opt}}\sim 4\gamma \tag{22}$$

It has been concluded that the optimal single-channel capacity with Fock-state coding equals [30]:

$$C_{\mathrm{Fock}}=(1+\bar{n})\ln(1+\bar{n})-\bar{n}\ln\ \bar{n} \tag{23}$$

which is the maximum capacity over all single channel communication schemes, Substituting Eq. (20) into Eq. (23) for large r we have:

$$C_{\mathrm{Fock}}\sim 2\gamma \tag{24}$$

This is just one-half of the asymptotic dense coding mutual information [Eq. (22)]. Thus asymptotically, at least, the dense coding scheme allows twice as much information to be encoded within a given state, although it has an extra expense of requiring shared entanglement. In Fig.6 we draw the function relations of the channel capacities versus $\bar{n}$ for comparing $C_{\mathrm{dc}}^{\mathrm{opt}}$ with a few of single-channel capacities for the mean photon number constraint, where [31—33]

$$C_{\mathrm{c}}=\ln\sqrt{1+4\bar{n}} \tag{25}$$

and

$$C_{\mathrm{ch}}=\ln(1+\bar{n}) \tag{26}$$

are the capacities of single-mode coherent state communication with the single-quadrature coding and single-homodyne detection (C_{c}) as well as the dual-quadrature coding and dual-homodyne (or hetrodyne) detection (C_{ch}), respectively.

$$C_{\mathrm{sh}}=\ln(1+2\bar{n}) \tag{27}$$

is the capacity of squeezed state communication with a single mode. From Fig. 6 we can see that the optimal channel capacity of the dense coding $C_{\mathrm{dc}}^{\mathrm{opt}}$ is always larger than C_{ch} and C_{c}. C_{sh} and C_{Fock} are beaten by the optimal dense coding scheme for $\bar{n}>0.478$ and $\bar{n}>1.88$, respectively .

It is worth noting that this dense coding scheme does not always beat the optimal single-channel capacity. Indeed, for small squeezing (small $\overline{n}$) it is worse. However, if we do not use the constraint condition for the optimal information capacity on $\overline{n}$ limited by Eq. (20) and Eq. (21), considering the general relation of Eq. (19) and increasing $\overline{n}$ by enhancing the intensity of the modulated signal (σ^2) for a given squeezing (r) the capacities of single channel communication can be beaten by the dense coding scheme at the lower squeezing level which is experimentally reachable at present.

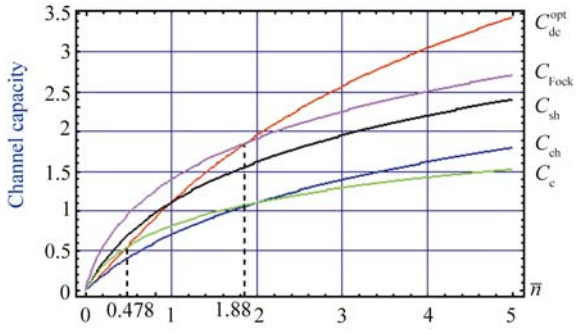

Fig. 6 The channel capacities for different communication schemes versus the mean number of photons.

5 Controlled dense coding using tripartite entanglement of continuous variables

Quantum entanglement shared by more than two parties is the essential base for developing quantum communication networks and quantum computation. The three-particle entangled state for DV, also called Greenberger-Horne-Zeilinger (GHZ) state, was proposed in 1990 [34] and then was experimentally realized at the end of the last century [35, 36]. Successively, a scheme to realize controlled dense coding of DV using GHZ state was proposed [37]. In the realm of CV, Loock and Braunstein firstly theoretically proved that the superposition of more than two independently squeezed states can yield multipartite entanglement for CV of an optical field and pointed out that even only one single-mode squeezed state distribution among N parties using linear optics sufficiently produce a truly N-partite entangled state for any nonzero squeezing and arbitrarily many parties [38]. Later, we proposed a scheme generating CV tripartite entangled state(also called it GHZ-like state of CV) by means of the bright two-mode squeezed state from NOPA and a protocol achieving CV-controlled dense coding based on CV tripartite entanglement [39]. According to this theoretical design, we obtained CV tripartite entangled state of light and demonstrated CV-controlled dense coding quantum communication in 2003 [40]. The value of the correlation variances measured in our experiments violated the separability criteria given in Ref. [41] and thus a fully inseparable CV tripartite entangled state was experimentally obtained.

Figure 7 is the schematic of the tripartite entangled state generation system. The entanglement source NOPA is operated at deamplification. The polarizations of two output optical modes from NOPA, $\hat{b}_1$ and $\hat{b}_2$, are oriented along the horizontal and vertical direction, respectively. Modes $\hat{b}_1$ and $\hat{b}_2$ are a pair of bright EPR entangled beams with anti-correlated amplitude quadratures and correlated phase quadratures. The coupled mode of $\hat{b}_1$ and $\hat{b}_2$ is a two-mode amplitude-quadrature squeezed state of light [27]. The polarizations of $\hat{b}_1$ and $\hat{b}_2$ are rotated by a half-wave plate (P_1), the optical axis of which is in $\theta_1 = 45^\circ - \frac{1}{2}\arcsin(\sqrt{2}-1)/\sqrt{6}$ relative to the horizontal direction, and then the beams pass through a polarizing-beam-splitter (PBS_1)with horizontal and vertical polarization. The output beam $\hat{b}'_2$ is split again by a 50/50 beam splitter (BS) consisting of a half-wave plate (P_2) and PBS_2 to modes $\hat{C}_2$ and $\hat{C}_3$. In Ref. [39], we have proved theoretically that the three optical modes $\hat{C}_1$, $\hat{C}_2$ and $\hat{C}_3$ are in a tripartite entangled state, which is a "three-mode position eigenstate" with the quantum correlations of total amplitude (position) quadratures ($\hat{X}_{C_1}$, $\hat{X}_{C_2}$ and $\hat{X}_{C_3}$) and relative phase (momentum) quadratures ($\hat{Y}_{C_1}$, $\hat{Y}_{C_2}$ and $\hat{Y}_{C_3}$). If distributing the outgoing tripartite entangled optical beams, $\hat{C}_1$, $\hat{C}_2$ and $\hat{C}_3$ to Alice, Bob and Claire, respectively, the channel capacity of dense coding communication between Alice and Bob can be controlled by Claire. The schematic of the controlled dense coding (CDC) system is shown in Fig. 8, where TES, BDM, D, SM, AM, and PM stand for the source of the tripartite entangled state, Bell-state direct measurement equipment, photodiode, spectrum analyzer, amplitude and phase modulator, respectively.

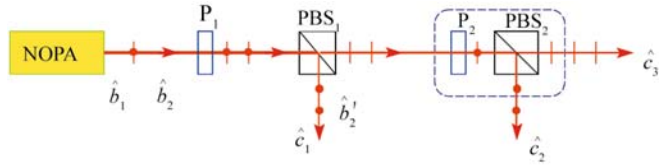

Fig. 7 The schematic of the tripartite entangled state generation system. NOPA: Nongenerate optical parametric amplifier; P_1 and P_2: Half-wave plate; PBS_1 and PBS_2: Polarizing-beam-splitter; $\hat{b}_1$ and $\hat{b}_2$: EPR optical beams from NOPA; $\hat{b}'_2$: Optical mode from PBS_1; $\hat{C}_1$, $\hat{C}_2$ and $\hat{C}_3$: Three entangled optical modes; • and |: Respectively showing the horizontal and vertical polarization of optical modes.

The sender Alice modulates two sets of classical signals X_s and Y_s on the amplitude and phase quadratures of her mode $\hat{c}_1$ by amplitude and phase modulators (AM and PM). The modulations lead to a displacement of a_s:

$$\hat{C}'_1 = \hat{C}_1 + a_{s_2} \tag{28}$$

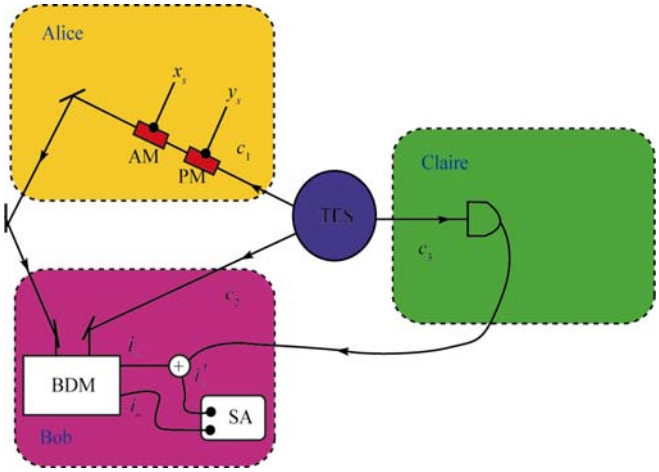

Fig. 8 Schematic for controlled dense coding quantum communication. TES: Source of tripartite entangled state; BDM: Bell-state direct measurement equipment; D: Photodiode; SM: Spectrum analyser; AM and PM: Amplitude and phase modulator.

where $a_s = X_s + \mathrm{i}Y_s$ is the sent signal via the quantum channel. The outgoing mode $\hat{C}'_1$ is sent to Bob who decodes the modulated signals with BDM under the aid of mode $\hat{C}_2$. Taking into account the imperfect detection efficiency of the photodiodes (η<1) and the nonzero losses of the optical systems (the transmission efficiency $\xi_1 < 1$ for $\hat{C}_1$ and $\hat{C}_2, \xi_2 < 1$ for $\hat{C}_3$), the noise power spectra of the sum and difference photocurrents of $\hat{C}_1$ and $\hat{C}_2$ modes are expressed by [39, 40]:

$$\left\langle \delta^2 \hat{i}_+ \right\rangle = \eta^2 \xi_1^2 \frac{\mathrm{e}^{2\gamma} + 8\mathrm{e}^{-2\gamma} - 9}{12} + 1 + \frac{1}{2} V_{X_s} \tag{29}$$

$$\left\langle \delta^2 \hat{i}_- \right\rangle = 3\eta^2 \xi_1^2 \frac{\mathrm{e}^{-2\gamma} - 1}{4} + 1 + \frac{1}{2} V_{Y_s} \tag{30}$$

where V_{X_s} and V_{Y_s} are the fluctuation variances of the modulated signals (X_s, Y_s). Claire detects the amplitude quadrature of mode $\hat{C}_3$ with a photodiode D and sends the measured photocurrent to Bob. Bob displaces Claire's result on the sum photocurrent to change $\hat{i}_+$ to $\hat{i}'_+$:

$$\begin{aligned}\hat{i}'_+ &= \hat{i}_+ + g\hat{i}_3 \\ &= \frac{\eta\xi_1}{\sqrt{2}}\left(\hat{X}_{C'_1} + \hat{X}_{C_2}\right) + g\eta\frac{\xi_2^2}{\xi_1}\hat{X}_{C_3} + \frac{\eta\sqrt{1-\xi_1^2}}{\sqrt{2}}\left(\hat{X}_{v_{C_1}} + \hat{X}_{v_{C_2}}\right) \\ &+ \frac{\sqrt{1-\eta^2}}{2}\left(\hat{X}_{v_{D_1}} + \hat{Y}_{v_{D_2}} + \hat{X}_{v_{D_2}} - \hat{Y}_{v_{D_2}}\right) \\ &+ \frac{g\eta\xi_2^2\sqrt{1-\xi_2^2}}{\xi_1}\hat{X}_{v_{C_3}} + \frac{g\xi_2\sqrt{1-\eta^2}}{\xi_1}\hat{X}_{v_{D_3}} + \frac{1}{\sqrt{2}}X_s \end{aligned} \tag{31}$$

where g describes the gain at Bob for the transformation from Claire's photocurrent to Bob's sum photocurrent. The optimal gain for attaining the minimum variances of the sum photocurrent is

$$g_{\mathrm{opt}} = \frac{(\mathrm{e}^{4\gamma} + 3\mathrm{e}^{2\gamma} - 4)\eta^2\xi_1^2}{\sqrt{2}(\mathrm{e}^{4\gamma}\eta^2\xi_2^2 - 3\mathrm{e}^{2\gamma}\eta^2\xi_2^2 + 6\mathrm{e}^{2\gamma} + 2\eta^2\xi_2^2)} \tag{32}$$

For an ideal case with perfect squeezing ($\gamma \to \infty$) and without losses ($\eta \to 1, \xi \to 1$), the optimal gain is $g_{\mathrm{opt}}^0 = \frac{1}{\sqrt{2}}$. For simplification and without losing generality, we take $g = \frac{1}{\sqrt{2}}$ in the following calculation and experiment, so the power fluctuation spectrum of the sum photocurrent of the three modes equals

$$\begin{aligned}\left\langle \delta^2 \hat{i}'_+ \right\rangle = \frac{1}{12}\Bigg\{ &\mathrm{e}^{2\gamma}\eta^2\left(\frac{\xi_2^2 - \xi_1^2}{\xi_1}\right)^2 + 2\mathrm{e}^{-2\gamma}\eta^2\left(\frac{\xi_2^2 + 2\xi_1^2}{\xi_1}\right)^2 \\ &- 3\left(\frac{\xi_2^4}{\xi_1^2}\eta^2 - 4 + 3\eta^2\xi_1^2 + 2\xi_2^2\eta^2 - 2\frac{\xi_2^2}{\xi_1^2}\right) + \frac{1}{2}V_{X_s}\Bigg\}\end{aligned} \tag{33}$$

Figure 9 shows the power fluctuation spectra measured in our CDC experiments. In Fig.9 (a), traces 2 and 3 are the noise spectra for the amplified sum photocurrents of two (trace 2 for $\left\langle \delta^2 \hat{i}_+ \right\rangle$) and three (trace 3 for $\left\langle \delta^2 \hat{i}'_+ \right\rangle$) optical modes, which are 2.7 dB and 1.0 dB below the SNL (trace 1), respectively. After the correction to the electronics noise floor, which is ~ 8 dB below the SNL (trace 4), noise reductions of $\left\langle \delta^2 \hat{i}'_+ \right\rangle$ and $\left\langle \delta^2 \hat{i}_+ \right\rangle$ relative to the SNL should be actually be 3.28 dB and 1.19 dB, respectively. In Fig.9 (b), trace 2 is the measured noise power spectrum of $\left\langle \delta^2 \hat{i}_- \right\rangle = \left\langle \delta^2 (Y_{c1} - Y_{c2}) \right\rangle$ for the relative phase correlation between modes C_1 and C_2, which is 2.66 dB below the SNL (trace 1). Accounting for the electronics noise (trace 3), it should be 3.18 dB below the SNL actually. Substituting the measured noise powers of $\left\langle \delta^2 \hat{i}_+ \right\rangle$, $\left\langle \delta^2 \hat{i}'_+ \right\rangle$ and $\left\langle \delta^2 \hat{i}_- \right\rangle$ into Eqs. (29)—(31), the squeezing parameter of $\gamma_{\mathrm{exp}} \approx 0.674$ is calculated. The parameters $\left\langle \delta^2 \hat{i}_+ \right\rangle$=0.76, $\left\langle \delta^2 \hat{i}_+ \right\rangle$=0.47, $\left\langle \delta^2 \hat{i}_- \right\rangle$ = 0.48, ξ_1^2=98.7 %, ξ_2^2=93.7 %, and η^2 = 95.0 % are taken in the calculation according to the experimental values.

The channel capacities with (C_c^{dense}) and without (C_{n-c}^{dense}) Claire's help can be deduced from the Eqs. (29), (30) and (33):

$$C_{n-c}^{\mathrm{dense}} = \frac{1}{2}\ln\left[\left(1 + \frac{\sigma^2}{\left\langle \delta^2 \hat{i}_- \right\rangle}\right)\left(1 + \frac{\sigma^2}{\left\langle \delta^2 \hat{i}_+ \right\rangle}\right)\right] \tag{34}$$

$$C_c^{\mathrm{dense}} = \frac{1}{2}\ln\left[\left(1 + \frac{\sigma^2}{\left\langle \delta^2 \hat{i}_- \right\rangle}\right)\left(1 + \frac{\sigma^2}{\left\langle \delta^2 \hat{i}'_+ \right\rangle}\right)\right] \tag{35}$$

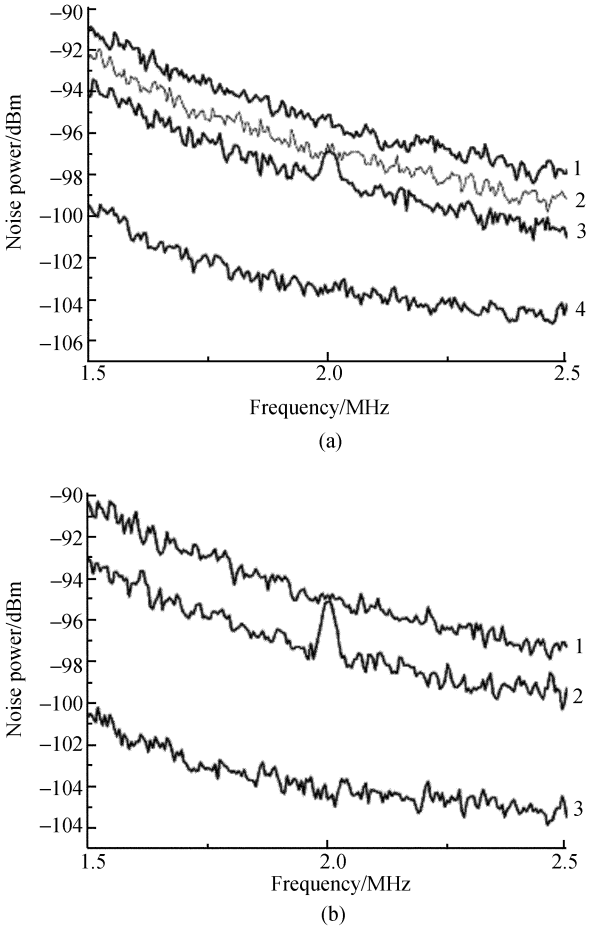

Fig. 9 **(a)** The noise power spectra of amplitude sums $\left\langle \delta^2 \hat{i}_+' \right\rangle$ (trace 3) and $\left\langle \delta^2 \hat{i}_+ \right\rangle$ (trace 2), trace 1: shot noise limit (SNL), trace 4: electronics noise level (ENL), measured frequency range 1.5−2.5 MHz, resolution bandwidth 30 kHz, video bandwidth 0.1 kHz. **(b)** The noise power spectra of phase difference $\left\langle \delta^2 \hat{i}_- \right\rangle$ (trace 2), trace 1: SNL, trace 3: ENL, measured frequency range 1.5−2.5 MHz, resolution bandwidth 30 kHz, video bandwidth 0.1 kHz.

where σ^2 is the average values of signal photon number and mean photon number per mode $\overline{n} = \sigma^2 + \sinh^2 \gamma$. For the given squeezing in our experiment ($\gamma_{\exp} = 0.674$), when the mean photon number $\overline{n}$ is larger than 1.00 (1.31), the C_c^{dense} (C_{n-c}^{dense}) will exceed C^{ch} and when $\overline{n}$ >10.52, C_c^{dense} will be larger than C^{sq}. By increasing the average signal photon number σ^2 , the channel capacity of the dense coding communication can be improved [29]. The channel capacity with the help of Claire (C_c^{dense}) is always larger than that without her help (C_{n-c}^{dense}), which is the result of the SNR improvement due to using the tripartite entanglement, For example, when $\overline{n}$ =11, the channel capacity of the presented system can be manipulated and inverted between 2.91 and 3.14.

6 Unconditional entanglement swapping

Due to exploiting entanglement, the quantum information encoded in nonorthogonal quantum states can be reliably transported by means of a special communication scheme called quantum teleportation. The teleportation of entangled states is the necessary basic step for establishing the quantum communication network and implementing the quantum computation. The term “entanglement swapping” was introduced for particularly characterizing the teleportation of the important quantum states, which means to entangle two quantum systems that have never directly interacted with each other. Unlike the entanglement swapping of discrete variables with single photons [14], where the postselection is a standard intrinsic procedure for overcoming the problem of probability in the detection of single photons [42], the entanglement swapping for continuous variables is unconditional in which the determinant EPR entanglement is used and thus the postselection is not needed. The unconditionality of CV quantum communication systems is hard to obtain in DV qubit-based implementations based on single photon states. In 1999, Tan [15], Loock, and Braunstein [16] independently proposed the protocols of CV entanglement swapping using the squeezed-state entanglement. Later, we designed the system of CV entanglement swapping based on a pair of bright ERP entanglement optical beams [17] and experimentally realized the unconditional entanglement swapping in 2004 [18].

The basic principle of CV entanglement swapping can be briefly expressed with Fig. 10. Initially, Alice and Bob own an independent entangled source (EPR) and there is no any quantum correlation between the two entangled states $(\hat{a}, \hat{b})$ and $(\hat{c}, \hat{d})$. However, if Alice and Bob respectively send a half of their own ERP beams, such as $\hat{b}$ and $\hat{c}$, respectively, to Claire, then Claire implements the joint Bell-state measurement on $\hat{b}$ and $\hat{c}$. In this case, the quantum information of mode $\hat{b}$ ($\hat{c}$) will be transferred to mode $\hat{d}$ ($\hat{a}$) due to the entanglement collapse resulting from the measurement and thus modes $\hat{a}$ and $\hat{d}$ will be entangled together although they have never directly interacted. In fact , if we ignore the mode $\hat{a}$ at firstf, Alice wants to teleport an unknown quantum states (mode $\hat{b}$) to Bob and asks Claire for her assistance. Claire implements the Bell-state measurement on modes $\hat{b}$ and $\hat{c}$, then sends the measured classical results of the amplitude and phase quadratures to Bob. Bob appropriately displaces the mode $\hat{d}$ with the obtained classical results to retrieve the quantum state of mode $\hat{b}$ on mode $\hat{d}$ as done in usual teleportation. We can say, the entanglement of modes $\hat{a}$ and $\hat{b}$ is swapped to modes $\hat{a}$ and $\hat{d}$ via a process of quantum teleportation of mode $\hat{b}$.

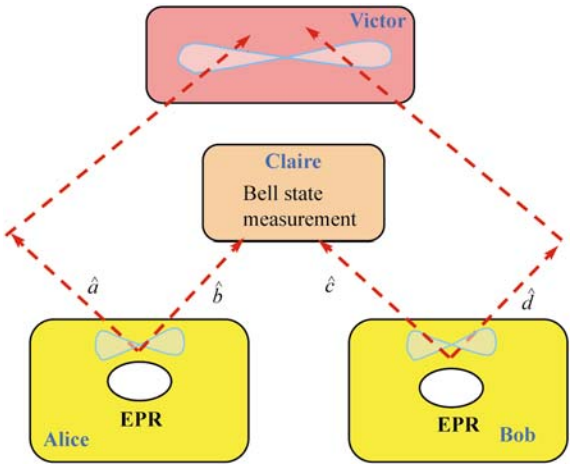

Fig.10 Basic scheme of CV entanglement swapping.

The experimental setup of CV entanglement swapping is shown schematically in Fig.11. The two NOPA pumped by a same Nd: YAP/KTP laser serve as the two independent entanglement sources. Both NOPAs were operated in the state of deamplification. Initially Alice and Bob own the entangled optical modes $\hat{a},\hat{b}$ and $\hat{c},\hat{d}$, respectively and they do not share entanglement. For establishing entanglement, Alice and Bob send their mode $\hat{b}$ and $\hat{c}$, respectively, to Claire. Claire performs a joint measurement of modes $\hat{b}$ and $\hat{c}$ by the direct detection of Bell-state. Claire's detection of modes $\hat{b}$ and $\hat{c}$ projects modes $\hat{a}$ and $\hat{d}$ on an inseparable entangled state, the entanglement of which is not changed by any local operation on mode $\hat{a}$ or $\hat{d}$ as classical displacement. The output mode $\hat{e}$ and $\hat{f}$ from the 50—50 beam splitter (BS1) in Claire are expressed by:

$$e=\frac{1}{\sqrt{2}}\eta\left[\left(\xi_1 b+\sqrt{1-\xi_1^2}v_b\right)+\mathrm{i}\left(\xi_1 c+\sqrt{1-\xi_1^2}v_c\right)\right]+\sqrt{1-\eta^2}v_e \tag{36}$$

$$f=\frac{1}{\sqrt{2}}\eta\left[\left(\xi_1 b+\sqrt{1-\xi_1^2}v_b\right)-\mathrm{i}\left(\xi_1 c+\sqrt{1-\xi_1^2}v_c\right)\right]+\sqrt{1-\eta^2}v_f \tag{37}$$

where η is the imperfect detection efficiency of the photodiodes (η<1) and we assume that the efficiency of all photodiodes used in the experimental system (D_1—D_4) are the same. ξ_1 is the transmission efficiency of mode $\hat{b}$ ($\hat{c}$) from NOPA1 (NOPA2) to BS1(ξ_1<1). v_b, v_c, and v_e, v_f correspond to the vacuum noises resulting from the imperfect mode-matching between mode $\hat{b}$ and $\hat{c}$ on BS1 and the imperfect detection efficiency of mode $\hat{e}$ and $\hat{f}$, respectively. The phase-shifter (PS) is used for ensuring the phase-difference of $\pi/2$ between mode $\hat{b}$ and $\hat{c}$ at BS1. The noise spectra of the sum (i_+^c) and the difference (i_-^c) of the photocurrents detected by D_1 and D_2 equal to:

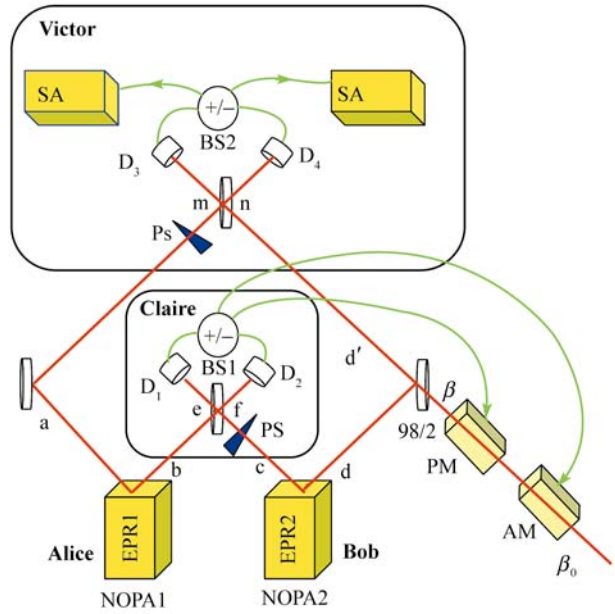

Fig. 11 Experimental setup of CV entangled swapping.

$$\begin{aligned} i_+^c(\Omega)=&\frac{1}{\sqrt{2}}[\eta\xi_1 X_b(\Omega)+\eta\xi_1 X_c(\Omega)\\ &+\eta\sqrt{1-\xi_1^2}X_{v_b}(\Omega)+\eta\sqrt{1-\xi_1^2}X_{v_c}(\Omega)]\\ &+\frac{1}{2}[\sqrt{1-\eta^2}X_{v_e}(\Omega)+\sqrt{1-\eta^2}X_{v_f}(\Omega)\\ &+\sqrt{1-\eta^2}Y_{v_e}(\Omega)-\sqrt{1-\eta^2}Y_{v_f}(\Omega)] \end{aligned} \tag{38}$$

$$\begin{aligned} i_-^c(\Omega)=&\frac{1}{\sqrt{2}}[\eta\xi_1 Y_b(\Omega)-\eta\xi_1 Y_c(\Omega)\\ &+\eta\sqrt{1-\xi_1^2}Y_{v_b}(\Omega)-\eta\sqrt{1-\xi_1^2}Y_{v_c}(\Omega)]\\ &+\frac{1}{2}[\sqrt{1-\eta^2}X_{v_e}(\Omega)-\sqrt{1-\eta^2}X_{v_f}(\Omega)\\ &+\sqrt{1-\eta^2}Y_{v_e}(\Omega)+\sqrt{1-\eta^2}Y_{v_f}(\Omega)] \end{aligned} \tag{39}$$

The classical information of the amplitude and phase quadratures of mode $\hat{b}$ and $\hat{c}$ are involved in i_+^c and i_-^c. For exhibiting the entanglement of mode $\hat{a}$ and $\hat{d}$, we send the photocurrents i_-^c and i_+^c to Bob through the classical channels. Bob implements the amplitude and phase modulation on a coherent state light β_0 with i_+^c and i_-^c by means of an amplitude (AM) and a phase (PM) modulator, respectively. The coherent light β_0 is a part divided from the fundamental wave of the laser source, and thus it has an identical frequency with the EPR beams at 1080 nm. The modulated optical mode β_0 becomes β:

$$\beta = \beta_0 + g_+ i_+^c(\Omega) + \mathrm{i}g_- i_-^c(\Omega) \tag{40}$$

The parameters g_+ and g_- describe the amplitude and phase gain for the transformation from photocurrent to output light field ($g_+ = g_- = g$ in the experiment for simplification). Then Bob combines mode $\hat{d}$ and $\hat{\beta}$ at a mirror Mr of reflectivity R = 98 %. In this manner the mode $\hat{d}$ is displaced to $\hat{d}'$:

$$\begin{aligned} d' = &\sqrt{R}(\xi_2 d + \sqrt{1-\xi_2^2}\, v_d) \\ &+\sqrt{1-R}[\beta_0 + g_+ i_+^c(\Omega) + \mathrm{i}g_- i_-^c(\Omega)] \end{aligned} \tag{41}$$

where ξ_2 and v_d are the imperfect transmission efficiency and vacuum noise introduced by losses of mode $\hat{d}$. If in spite of mode $\hat{a}$, the process is a quantum teleportation of mode $\hat{b}$ from Claire to Bob based on exploiting the entanglement between modes $\hat{c}$ and $\hat{d}$ [16], then the quantum state of mode $\hat{b}$ is the teleported input state and Claire corresponds to the sender (Alice) in a normal teleportation system [7]. Claire's Bell-state detection on mode $\hat{b}$ and $\hat{c}$ collapses Bob's mode $\hat{d}$ into a state conditioned on the measurement outputs (i_+^c, i_-^c). Hence, after receiving the classical information from Claire, Bob is able to reconstruct the teleported state $\hat{b}$ via a simple phase-space displacement of mode $\hat{d}$. To verify that the entanglement swapping has been accomplished, we implement the direct Bell-state measurement of mode $\hat{a}$ and $\hat{d}'$. The output modes $\hat{m}$ and $\hat{n}$ from the 50—50 beam splitter BS2 are expressed by:

$$\begin{aligned} m = \frac{1}{\sqrt{2}}\eta\Big[&\Big(\xi_3 a + \sqrt{1-\xi_3^2}\, v_a\Big) \\ &+\mathrm{i}\Big(\xi_4 d' + \sqrt{1-\xi_4^2}\, v_{d'}\Big)\Big] + \sqrt{1-\eta^2}\, v_m \end{aligned} \tag{42}$$

$$\begin{aligned} n = \frac{1}{\sqrt{2}}\eta\Big[&\Big(\xi_3 a + \sqrt{1-\xi_3^2}\, v_a\Big) \\ &-\mathrm{i}\Big(\xi_4 d' + \sqrt{1-\xi_4^2}\, v_{d'}\Big)\Big] + \sqrt{1-\eta^2}\, v_n \end{aligned} \tag{43}$$

where, ξ_3 and ξ_4 are the transmission efficiency of mode $\hat{a}$ and $\hat{d}'$, respectively. v_a and $v_{d'}$ are the vacuum noise introduced by the losses of mode $\hat{a}$ and $\hat{d}'$, respectively. v_m and v_n stand for the vacuum noise on mode $\hat{m}$ and $\hat{n}$ from the imperfect detection efficiency of the photodiode D_3 and D_4, respectively. The noise spectra of the sum and the difference of the photocurrents detected by D_3 and D_2 respectively are equal to:

$$\begin{aligned} i_+^v(\Omega) = \frac{1}{\sqrt{2}}[&\eta\xi_3 X_a(\Omega) + \sqrt{R}\eta\xi_2\xi_4 X_d(\Omega) + \eta\sqrt{1-\xi_3^2}\, X_{v_a}(\Omega) \\ &+\sqrt{R}\eta\sqrt{1-\xi_2^2}\,\xi_4 X_{v_d}(\Omega) + \eta\sqrt{1-\xi_4^2}\, X_{v_{d'}}(\Omega) \\ &+\sqrt{1-R}\eta\xi_4 X_{\beta 0}(\Omega) + \sqrt{1-R}\eta g_+ \xi_4 i_+^c(\Omega)] \\ &+\frac{1}{2}[\sqrt{1-\eta^2}\, X_{v_m}(\Omega) + \sqrt{1-\eta^2}\, X_{v_n}(\Omega) \\ &+\sqrt{1-\eta^2}\, Y_{v_m}(\Omega) - \sqrt{1-\eta^2}\, Y_{v_n}(\Omega)] \end{aligned} \tag{44}$$

$$\begin{aligned} i_-^v(\Omega) = \frac{1}{\sqrt{2}}[&\eta\xi_3 Y_a(\Omega) - \sqrt{R}\eta\xi_2\xi_4 Y_d(\Omega) + \eta\sqrt{1-\xi_3^2}\, Y_{v_a}(\Omega) \\ &-\sqrt{R}\eta\sqrt{1-\xi_2^2}\,\xi_4 Y_{v_d}(\Omega) - \eta\sqrt{1-\xi_4^2}\, Y_{v_{d'}}(\Omega) \\ &-\sqrt{1-R}\eta\xi_4 Y_{\beta 0}(\Omega) - \sqrt{1-R}\eta g_- \xi_4 i_-^c(\Omega)] \\ &+\frac{1}{2}[\sqrt{1-\eta^2}\, X_{v_m}(\Omega) - \sqrt{1-\eta^2}\, X_{v_n}(\Omega) \\ &+\sqrt{1-\eta^2}\, Y_{v_m}(\Omega) + \sqrt{1-\eta^2}\, Y_{v_n}(\Omega)] \end{aligned} \tag{45}$$

Using the input and output relations of NOPA expressed in Eq. (1), we can calculate the variances of the sum and the difference photocurrents:

$$\begin{aligned} \left\langle \delta^2 i_+^v \right\rangle &= \left\langle \delta^2 i_-^v \right\rangle \\ &= \frac{1}{4}(\eta\xi_3 - g_{\mathrm{swap}}\eta\xi_4)^2 \mathrm{e}^{2r_1} + \frac{1}{4}(\sqrt{R}\eta\xi_2\xi_4 \\ &\quad - g_{\mathrm{swap}}\eta\xi_4)^2 \mathrm{e}^{2r_2} + \frac{1}{4}(\eta\xi_3 + g_{\mathrm{swap}}\eta\xi_4)^2 \mathrm{e}^{-2r_1} \\ &\quad + \frac{1}{4}(\sqrt{R}\eta\xi_2\xi_4 + g_{\mathrm{swap}}\eta\xi_4)^2 \mathrm{e}^{-2r_2} + 1 - \eta^2 \\ &\quad + \frac{1}{2}\eta^2(2 - \xi_3^2 - \xi_4^2) + \frac{1}{2}(1 - R\xi_2^2)\eta^2\xi_4^2 \\ &\quad + \frac{g_{\mathrm{swap}}^2(1-\eta^2\xi_1^2)\xi_4^2}{\xi_1^2} \end{aligned} \tag{46}$$

where $g_{\mathrm{swap}} = \frac{1}{\sqrt{2}}\sqrt{1-R}\eta\xi_1 g_{+(-)}$ is the normalized gain factor. Minimizing Eq. (46) we get the optimum gain factor for the maximum entanglement of mode $\hat{a}$ and $\hat{d}'$:

$$\begin{aligned} g_{\mathrm{swap}}^{\mathrm{opt}} = &\eta^2[(\mathrm{e}^{4r_1} - 1)\mathrm{e}^{2r_2}\xi_3 + \mathrm{e}^{2r_1}(\mathrm{e}^{4r_2} - 1)\sqrt{R}\xi_2\xi_4]\xi_1^2 \\ &/\Big\{4\mathrm{e}^{2(r_1+r_2)} + \eta^2[\mathrm{e}^{2r_1} + \mathrm{e}^{2r_2} + \mathrm{e}^{4r_1+2r_2} \\ &+\mathrm{e}^{2r_1+4r_2} - 4\mathrm{e}^{2(r_1+r_2)}]\xi_1^2\Big\}\xi_4 \end{aligned} \tag{47}$$

Substituting the actual correlation parameters of the two initial EPR beams ($\hat{a}$, $\hat{b}$) and ($\hat{c}$, $\hat{d}$), r_1 = 0.564 (4.9 dB below the SNL) and r_2 = 0.587 (5.1 dB below the SNL), into Eq. (47), we have $g_{\mathrm{swap}}^{\mathrm{opt}} = 0.74$ ($\xi_1^2 = 0.970, \xi_2^2 = 0.950, \xi_3^2 = 0.966, \xi_4^2 = 0.968, \eta^2 = 0.90$ and $R = 0.98$ correspond to the real parameters of our experimental system). According to the optimum gain value, the classical channels from Claire to Bob should be carefully adjusted in a manner de-

scribed in Ref. [43] to the optimum value.

Figures 12 (a) and (b) are the noise power spectra of the joint Bell-state measurement of mode $\hat{a}$ and $\hat{d}'$. The trace 4 in Fig.12 (a) and (b) are the measured correlation noise powers of the amplitude sum, $\left\langle \delta^2 \left(X_a + X_{d'} \right) \right\rangle$, and the phase difference, $\left\langle \delta^2 \left(Y_a - Y_{d'} \right) \right\rangle$, at the sideband mode of 2 MHz, respectively, both of which are below the corresponding SNL (trace3). The anti-correlation of the amplitude quadratures and the correlation of the phase quadratures are 1.23 dB and 1.12 dB below the SNL, respectively. The trace 1 in Figs.12 (a) and (b) are the noise power spectra of the amplitude sum and the phase difference of mode $\hat{a}$ and $\hat{d}'$ when the classical channels of i_+^c and i_-^c from Claire to Bob are blocked, which are much higher than traces 4 and also the SNL (traces 3). It verifies clearly the conclusion of Ref. [16] that the entanglement of mode a and d' cannot be exhibited and used without the assistance of Claire's measurement results. Even the amplitude noises of single-mode $\hat{a}$ [trace 2 in Fig. 12(a)] and mode $\hat{d}'$ [trace 2 in Fig.12 (b)] are higher than the correlation noises of two modes and the SNL. The results agree with the characteristics of EPR entangled light [23]. The measured results show that the quantum entanglement between mode $\hat{a}$ and $\hat{d}'$ ($\hat{d}$), which have never interacted with each other, is truly established during the operation of the entanglement swapping. Due to the influences of the imperfect transmission and detection efficiencies, the initial entanglement of mode $\hat{a}$ and $\hat{b}$ (4.9 dB below the SNL) cannot be fully preserved. The percentage of the entanglement preserved after swapping with respect to the initial entanglement value is about 29 %.

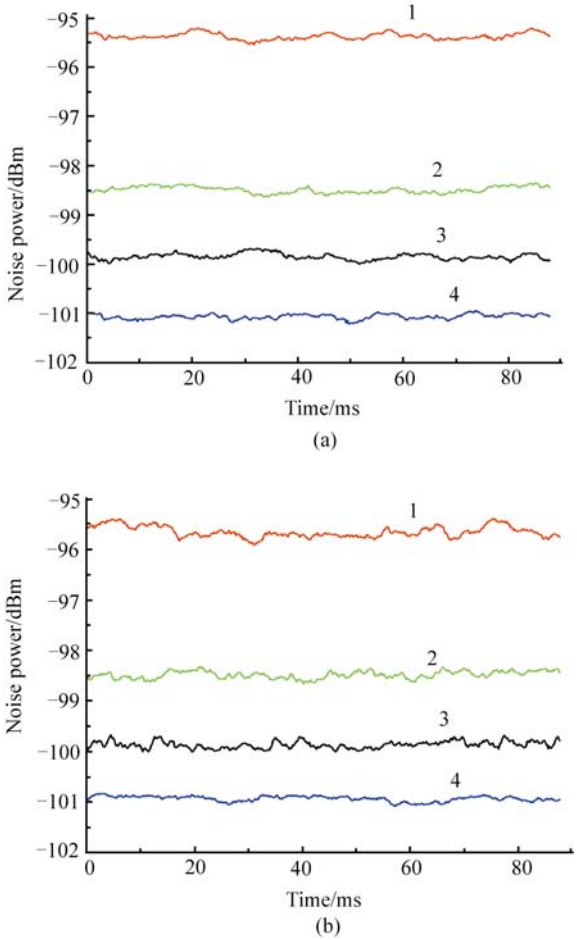

Fig. 12 The correlation noise powers resulting from entanglement swapping at 2 MHz as a function of time. **(a)** 1, the noise power of the amplitude sum without the classical information from Claire; 2, the noise power of amplitude of mode $\hat{a}$; 3, SNL;4, the correlation noise power of the amplitude sum with the classical information from Claire. **(b)** 1, The noise power of the phase difference without the classical information from Claire; 2, The noise power of amplitude of mode $\hat{d}$; 3, SNL; 4, The correlation noise power of the phase difference with the classical information from Claire. The measurement parameters of SA: Resolution bandwidth is 10 kHz; Video bandwidth is 30 Hz.

7 Conclusions

We achieved quantum dense coding, controlled dense coding, and entanglement swapping for continuous variables by exploiting the determinant entanglement of the bright EPR optical beams produced from $NOPA_S$ and the Bell-state direct detection. The long-term intensity and frequency stability of the laser pump sources (Nd: YAP/KTP laser) and the thermal stabilities of the $NOPA_S$ are the important requirements for demonstrating these experiments. The experiments show the potential of CV entanglement in the application of unconditional signal transmission with high efficiency. CV implementations work "always" pretty well (efficiently and unconditionally), but never perfectly due to finite EPR correlation degrees available in experiments and the sensitivity of entanglement to losses. A variety of attractive applications of CV entanglement have been demonstrated in principle so far. It might be important to improve significantly the quality of entanglement sources and to explore the effective schemes of entanglement distribution for developing CV quantum communication over long distances.

References

1. Bouweester D., Ekert A., and Zeilinger A. (Eds.), The Physics of Quantum Information, Springer, 2001
2. Braunstein S. L. and Pati A.K. (Eds.), Quantum Information with Continuous Variables, Kluwer Academic Publishers, 2003
3. Bennett C. H., et al., Phys. Rev. Lett., 1993, 70: 1895
4. Vaidmann L., Phys. Rev.A,1994,49: 1473
5. Braunstein S. L. and Kimble H. J., Phys. Rev, Lett., 1998, 80: 869
6. Bouwmeester, et al., Nature (London) ,1997, 390: 575
7. Furusawa A., et al., Science,1998, 282: 706
8. Bennett C. H. and Wiesner S. L., Phys. Rev. Lett.,1992,9:2881
9. Mattle K., Weinfurter H., Kwiat P. G.,and Zeilinger A., Phys. Rev.

Lett.,1996,6:4656
10. Braunstein S. L. and Kimble H. J., Phys. Rev. A,2000,1:042302
11. Zhang J. and Peng K. C., Phys. Rev. A,2000,62: 064302
12. Li Xiao-ying, Pan Qing, Jing Jie-tai, Zhang J, Xie Chang-de, and Peng Kun-chi, Phys. Rev. Lett., 2002, 88: 047904
13. Zukowski M., Zeilinger A., Horne M. A.,and Ekert A. K., Phys. Rev. Lett., 1993, 71: 4287
14. Pan J. W., et al., Phys. Rev. Lett., 1998, 80: 3891
15. Tan S. M., Phys. Rev. A,1999,60: 2752
16. Loock P. Van, et al., Phys. Rev. A,1999,61: 010302R
17. Zhang Jing, Xie Chang-de,and Peng Kun-chi, Phys. Lett. A,2002, 299: 427
18. Jia Xiao-jun, Su Xiao-long, Pan Qing, Gao Jiang-rui, Xie Chang-de, and Peng Kun-chi, Phys. Rev. Lett.,2004,93: 250503
19. Wang Xiang-bin, et al., Frontiers of Physics in China, 2006,1(3):251
20. Zeng He-ping, et al., Frontiers of Physics in China, 2006,1(1):1
21. Yonezawa H., Aoki T., and Furusawa A., Nature,2004, 431: 430
22. Lance M. A, Symul T., Bowen P. W., Sanders C. B.,and Lam P. K., Phys. Rev. Lett.,2004,90: 177903
23. Reid M. D. and Drammond P. D., Phys. Rev. Lett.,1988,60: 2731
24. Reid M. D., Phys. Rev. A,1989, 40: 913
25. Qu Z. Y., Pereira S. F., Kimde H. J.,and Peng K. C., Phys. Rev. Lett.,1992,68: 3663
26. Zhang Y., Wang H., Li X. Y., Jing J. T., Xie C. D., and Peng K. C., Phys. Rev. A, 2000, 62: 023813
27. Zhang Y., Su H., Xie C. D.,and Peng K. C., Phys. Lett. A, 1999, 259: 171
28. Li X. Y., Pan Q., Jing J. T., Xie C. D.,and Peng K. C., Optics Communication, 20001, 01: 01685－6
29. Ralph T. C. and Huntington E. H., Phys. Rev. A, 2002, 66: 04231
30. Caves C. M. and Drummond P. D., Rev. Mod. Phys., 1994, 66: 481
31. Gordon J. P., Proc. IRE, 1962, 50: 1898
32. She C. Y., IEEE Trans. Inf. Theory, 1968, IT-14: 32
33. Yamamoto Y. and Haus H. A., Rev. Mod. Phys., 1986, 58: 1001
34. Greenberger D. M., et al., Am. J. Phys., 1990, 58: 1131
35. Bouwmeester D., et al., Phys. Rev. Lett., 1999, 82: 1345
36. Laflamme, et al., Philos. Trans. R. Soc. London A, 1998, 356: 1941
37. Hao J. C., Li C. F., and Guo G. C., Phys. Rev. A, 2001, 63: 054301
38. Loock P. V. and Braunstein S. L., Phys. Rev. Lett., 2000, 84: 3482
39. Zhang Jing, Xie Chang-de, and Peng Kun-chi, Phys. Rev. A, 2002, 66: 032318
40. Jing Jie-tai, Zhang Jing, Yan Ying, Zhao Fa-gang, Xie Chang-de, and Peng Kun-chi, Phys. Rev. Lett., 2003, 90: 167903
41. Loock P. V. and Furusawa A., Phys. Rev. A, 2003, 67: 052315
42. Ch. Silberhorn, et al., Phys. Rev. Lett., 2002, 89: 167901
43. Zhang T. C., et al., Phys. Rev. A, 2003, 67: 033802